

## Article

# PbS<sub>1-x</sub>Se<sub>x</sub>-Quantum-Dot@MWCNT/P3HT Nanocomposites with Tunable Photoelectric Conversion Performance

He Zhu <sup>1,2</sup>, Huilin Hu <sup>1</sup>, Minheng Ye <sup>1,2</sup>, Jinhua Ye <sup>1,2,3</sup> and Defa Wang <sup>1,2,\*</sup>

- <sup>1</sup> TJU-NIMS International Collaboration Laboratory, Key Laboratory of Advanced Ceramics and Machining Technology (Ministry of Education), Tianjin Key Laboratory of Composite and Functional Materials, School of Materials Science and Engineering, Tianjin University, 92 Weijin Road, Tianjin 300072, China; longziyudl@163.com (H.Z.); huhuulin@tju.edu.cn (H.H.); yeminheng@tju.edu.cn (M.Y.); jinhua.ye@nims.go.jp (J.Y.)
- <sup>2</sup> Collaborative Innovation Center of Chemical Science and Engineering, 92 Weijin Road, Tianjin 300072, China
- <sup>3</sup> International Center for Materials Nanoarchitectonics (WPI-MANA), National Institute for Materials Science (NIMS), Namiki 1-1, Tsukuba 305-0044, Japan
- \* Correspondence: defawang@tju.edu.cn



**Citation:** Zhu, H.; Hu, H.; Ye, M.; Ye, J.; Wang, D. PbS<sub>1-x</sub>Se<sub>x</sub>-Quantum-Dot@MWCNT/P3HT Nanocomposites with Tunable Photoelectric Conversion Performance. *Inorganics* **2021**, *9*, 87. <https://doi.org/10.3390/inorganics9120087>

Academic Editor: Antonino Gulino

Received: 2 November 2021

Accepted: 7 December 2021

Published: 10 December 2021

**Publisher's Note:** MDPI stays neutral with regard to jurisdictional claims in published maps and institutional affiliations.



**Copyright:** © 2021 by the authors. Licensee MDPI, Basel, Switzerland. This article is an open access article distributed under the terms and conditions of the Creative Commons Attribution (CC BY) license (<https://creativecommons.org/licenses/by/4.0/>).

**Abstract:** The photoelectric performance of quantum dots (QDs)-based nanocomposites is closely related to the optical properties of QDs, which play a critical role in the optical absorption and separation/transfer of charge carriers. Herein, we report a nanocomposite composed of light absorber PbS<sub>1-x</sub>Se<sub>x</sub> quantum dots (QDs), electron-conducting multiwalled carbon nanotubes (MWCNTs) and hole-conducting poly-3-hexylthiophene (P3HT) with tunable photoelectric conversion performance. In addition to using the quantization effect, we proposed solid-solution PbS<sub>1-x</sub>Se<sub>x</sub> QDs ( $x = 0, 0.25, 0.5, 0.75, 1$ ) for band gap engineering. In particular, we successfully synthesized relatively small (~5.3 nm) and uniform QDs via the hot-injection method by using PbCl<sub>2</sub>, S/Se powder and environmentally friendly oleylamine (OLA) as the precursors and/or solvent. By increasing the content of Se, the band gap of PbS<sub>1-x</sub>Se<sub>x</sub> QDs decreased along with the decrease in the conduction band and valence band edges. The suitable energy level alignment enabled the efficient transfer of photoinduced charge carriers, and hence a much higher photoelectric conversion performance of the PbS<sub>1-x</sub>Se<sub>x</sub>-QD@MWCNT/P3HT nanocomposites than the individual QDs, P3HT, and binary PbS<sub>1-x</sub>Se<sub>x</sub>-QD@MWCNT, as well as the best performance, was achieved over PbS<sub>0.75</sub>Se<sub>0.25</sub>-QD@MWCNT/P3HT.

**Keywords:** PbS<sub>1-x</sub>Se<sub>x</sub> quantum dot; multiwalled carbon nanotube; P3HT; nanocomposite; charge transfer; photoelectric conversion

## 1. Introduction

Colloidal quantum dots (QDs) have attracted a great deal of attention for photoelectric conversion owing to their excellent electronic properties [1–4]. Among the various QDs, lead chalcogenide QDs such as PbS [5,6] and PbSe [7–9] are of particular interest due to their specific advantages such as narrow band gaps (bulk PbS: 0.41 eV; bulk PbSe: 0.28 eV) and large exciton Bohr radii (~18 nm for PbS; ~46 nm for PbSe) [10,11], which provide a high possibility to extend light harvesting into the entire near-infrared region via the shape- and/or size-related quantization effect. Moreover, the large molar extinction coefficient, high carrier mobility and multiple exciton generation effect (MEG) [12] in lead chalcogenides QDs could further enhance the overall photoelectric conversion efficiency (PCE).

Lead chalcogenide QDs are usually synthesized by the well-developed colloidal synthetic route, showing a relatively monodisperse size distribution, clear and discrete optical transition and high fluorescence quantum yield [4,13,14]. However, as-synthesized lead chalcogenide QDs are often passivated with ~2.5 nm long insulating oleate ligands

(e.g., OLA), which impede efficient charge carrier transport among the QDs in a film. In fact, the abundant interfaces in the random network of QDs increase the probability of recombination of photoinduced electrons and holes, seriously limiting the transport of photoinduced charge carriers to the electrodes of QD-based solar cells. To improve the photoelectric property of PbS/PbSe-QD films, ligand exchange is usually employed to replace the long oleate ligands with short ones such as various amines (e.g., *n*-butylamine [5,15] or methylamine [8]) and/or thiols (e.g., ethanedithiol or benzenedithiol [6,7]). However, the ligand exchange is a very laborious and time-consuming process, which involves repeated solution precipitation and easily leads to agglomeration of the original QDs. An effective method has been developed by properly coupling QDs with other materials for conducting electrons (e.g., multiwalled carbon nanotubes (MWCNTs), graphene, etc.) or holes (e.g., organic conjugated polymers such as P3HT) so as to form an efficient bulk heterojunction [16–23]. In this context, we previously developed a two-step solution process to fabricate the P3HT:PbS-QD/MWCNT nanocomposite, which exhibited significantly enhanced photoelectric conversion efficiency, while the fairly complicated ligand-exchange procedure was not necessary [17].

It is worth recognizing that the electronic property of QDs usually plays a critical role in regulating the optical absorption, transfer of charge carriers and hence the photoelectric conversion performances of QD-based nanocomposites [24–26]. However, narrowing of the band gap of QDs via the size quantization effect is mainly due to the decrease in the conduction band (CB) bottom while the valence band (VB) top increases slightly [20,27]. Our previous study on the PbS-QDs/TiO<sub>2</sub> composite system demonstrated that the PbS QDs must be smaller than a critical size to maintain the conduction band (CB) edge higher than that of the TiO<sub>2</sub> so that the photoinduced electrons produced by PbS QDs could be transferred to TiO<sub>2</sub> [25]. In addition to the size-related quantization effect, making solid-solution semiconductors has been proved to be an alternative approach to tuning the energy band structure, from which the derived properties are unattainable by either of the individual end materials [28–36].

The different band gaps (bulk PbS: 0.41 eV; bulk PbSe: 0.28 eV) and the different exciton Bohr radii (PbS: ~18 nm; PbSe: ~46 nm) [10,11] would allow us to be able to tune the electronic structure of PbS<sub>1-x</sub>Se<sub>x</sub> solid-solution QDs to a large extent while maintaining the large Bohr radius and the MEG effect [12]. For a given particle size, PbSe QDs have a relatively smaller band gap than PbS QDs, and both the CB and VB edges of PbSe QDs are lower than those of PbS QDs [37,38]. More importantly, previous reports showed that the integration of ternary PbS<sub>1-x</sub>Se<sub>x</sub> QDs into solar cells could simultaneously optimize both the carrier transport and the voltage and hence further increase the photoelectric conversion efficiency (PCE) [26,37].

As for the synthesis of high-quality lead chalcogenide QDs, toxic phosphorous surfactants such as trioctylphosphine (TOP) or tributylphosphine (TBP) and air-sensitive bis(trimethylsilyl) sulfide (TMS-S) or bis(trimethylsilyl) selenide (TMS-Se) were usually used [1,4,29,39]. Alternatively, a more environment-friendly green method has been developed for the synthesis of lead chalcogenide QDs by using OLA as both the ligand and solvent, as OLA is more advantageous in cutting costs, avoiding pollution and supporting the large-scale synthesis over the other ligands and solvents as mentioned above [13,14,40,41]. However, the size of previously reported PbS<sub>x</sub>Se<sub>1-x</sub> solid-solution QDs synthesized using this method was quite large (10–12 nm) [30]. It is known that the high PCE requires not only a suitable optical absorption but also a high open-circuit voltage realized by small-sized QDs [3,42].

In this paper, we synthesized uniform small-sized PbS<sub>1-x</sub>Se<sub>x</sub> ( $x = 0, 0.25, 0.5, 0.75, 1$ ) solid-solution QDs (~5.3 nm) by using PbCl<sub>2</sub> and S/Se powder with oleylamine (OLA) as the sole ligand and solvent. The as-synthesized PbS<sub>1-x</sub>Se<sub>x</sub> QDs were attached to the OLA-functionalized MWCNTs and further mixed with a hole-conducting polymer poly-3-hexylthiophene (P3HT) to construct the PbS<sub>1-x</sub>Se<sub>x</sub>-QD@MWCNT/P3HT nanocomposite, in which the PbS<sub>1-x</sub>Se<sub>x</sub> QDs acted as the light absorber, while MWCNTs and P3HT served

as the electron conductor and hole conductor, respectively. The photoelectric conversion performances of  $\text{PbS}_{1-x}\text{Se}_x\text{-QD@MWCNT/P3HT}$  nanocomposites were investigated by the amperometry, and the highest photocurrent intensity was obtained over  $\text{PbS}_{0.75}\text{Se}_{0.25}\text{-QD@MWCNT/P3HT}$ . The influence of composition-induced variations in the band gap and band edges of QDs on the photoelectric conversion performance of the  $\text{PbS}_{1-x}\text{Se}_x\text{-QD@MWCNT/P3HT}$  nanocomposites was discussed accordingly. Our work provides a feasible strategy for the development of highly efficient photoelectric conversion devices by properly integrating QDs, CNTs and polymers into a nanocomposite.

## 2. Results and Discussion

Figure 1a–e presents the TEM and high-resolution TEM (HRTEM) images of the synthesized  $\text{PbS}_{1-x}\text{Se}_x$  QDs with different  $x$  values. While S and Se possessed different reaction activities in the synthesis process, all the  $\text{PbS}_{1-x}\text{Se}_x$  QDs were grown in nearly spherical shapes irrespective of the different  $x$  values. The QD sizes were also well controlled to be around 5.0–5.5 nm (5.46 nm for  $x = 0$ , 5.03 nm for  $x = 0.25$ , 5.3 nm for  $x = 0.50$ , 5.5 nm for  $x = 0.75$  and 5.34 nm for  $x = 1$ ) with a relatively uniform distribution, as evidenced by the histogram of size distribution (Figure S1, Supporting Information). Moreover, the HRTEM images (insert) demonstrate the high crystallinity of  $\text{PbS}_{1-x}\text{Se}_x$  QDs. We need to mention that the replacement of S with Se expanded the lattice spacing of the (200) plane from 2.95 Å to 3.05 Å, which was in good agreement with Vegard's law [30,37,43]. The typical XRD patterns of  $\text{PbS}_{1-x}\text{Se}_x$  QDs are shown in Figure 1f. Unlike the bulk materials, the broader peaks of  $\text{PbS}_{1-x}\text{Se}_x$  QDs could be ascribed to the nanosize effect and nonuniform strain in QDs [29]. Nonetheless, the diffraction peaks of the (111), (200) and (220) planes from the  $\text{PbS}_{1-x}\text{Se}_x$  solid-solution QDs could be assigned well to the halite structures of PbS (JCPDS #05-0592) and PbSe (JCPDS #06-0354) [29,30], while the diffraction peaks of the solid-solution  $\text{PbS}_{1-x}\text{Se}_x$  QDs were in between the lattice parameters of PbS and PbSe. The XRD peaks can be found to shift to a lower angle with higher  $x$  values since the radius of  $\text{Se}^{2-}$  (0.198 nm) is larger than that of  $\text{S}^{2-}$  (0.184 nm).

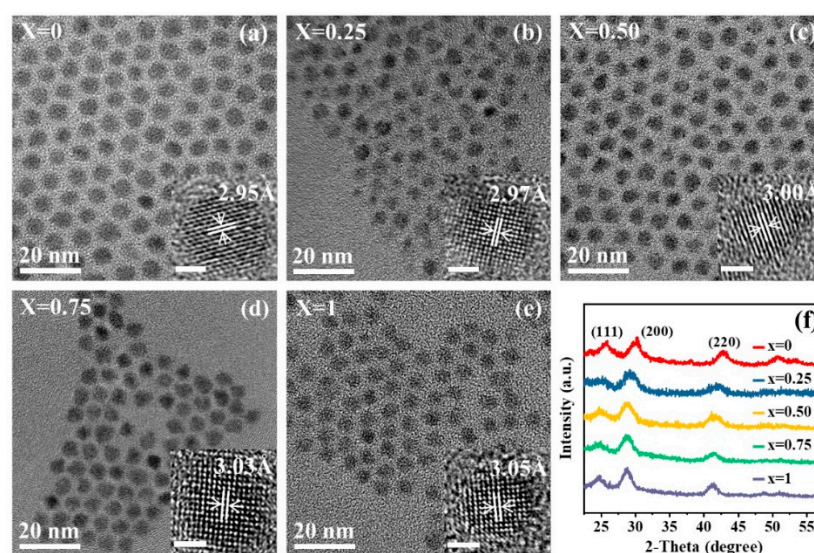


**Figure 1.** (a–e) TEM and HRTEM images (insert, scale bar: 2 nm) of  $\text{PbS}_{1-x}\text{Se}_x$  QDs. (f) XRD patterns of  $\text{PbS}_{1-x}\text{Se}_x$  QDs.

The absorption and PL spectra of  $\text{PbS}_{1-x}\text{Se}_x$  QDs are displayed in Figure 2. All the first excitation peaks appeared clearly on the absorption spectra, as shown in Figure 2a. The small spurious peak located at ~1418 nm might originate from OLA, as many similar reports have shown that the optical properties of QDs could be influenced by the bonded ligand on the surface [44–47]. Using Gaussian fitting (Figure S2), the first excitation peak of PbS QDs was identified to be at 1410 nm, and the replacement of S with Se gradually shifted

the peak position to the long-wavelength region (1538 nm for PbSe QDs). Accordingly, the PL peaks of  $\text{PbS}_{1-x}\text{Se}_x$  QDs shifted from 1423 nm ( $x = 0$ ) to 1596 nm ( $x = 1$ ). Based on the absorption and PL spectra, the band gaps of  $\text{PbS}_x\text{Se}_{1-x}$  QDs were estimated to be narrowed from 0.879 eV ( $x = 0$ ) to 0.806 eV ( $x = 1$ ). Apparently, the optical property of  $\text{PbS}_{1-x}\text{Se}_x$  QDs was successfully tuned by simply varying the solid-solution composition while keeping the similar size of QDs [29,48]. Increasing the content of Se led to red-shift of the absorption edge and PL peak of  $\text{PbS}_{1-x}\text{Se}_x$  QDs.

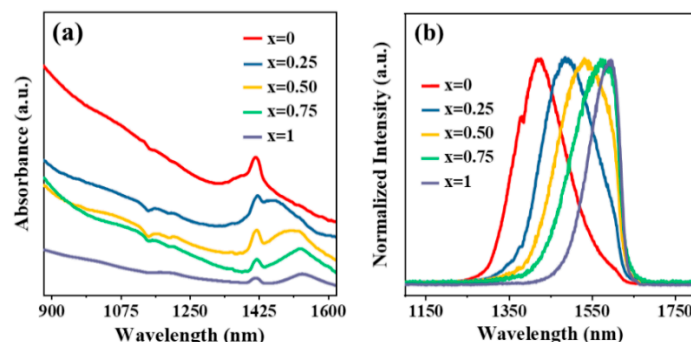


**Figure 2.** (a) Absorption spectra (offset for clarity) and (b) PL spectra of  $\text{PbS}_{1-x}\text{Se}_x$  QDs.

Figure 3a,b shows the TEM images of  $\text{PbS}_{0.75}\text{Se}_{0.25}\text{-QD@MWCNT}$  nanoarchitecture constructed by using OLA as the bonding agent. We can see that the hydrophobic interaction between OLA molecules enabled tight attachment of OLA-covered QDs to OLA-functionalized MWCNTs. It was interesting to see that, as shown in Figure 3c, the PL intensity of  $\text{PbS}_{0.75}\text{Se}_{0.25}\text{-QD@MWCNT}$  was much lower than that of  $\text{PbS}_{0.75}\text{Se}_{0.25}$  QDs, indicating the promoted transfer of photoinduced electrons from QDs to MWCNTs with a perfect ballistic conductivity. Compared with pure QDs, the slight blue-shift of the PL peak of QD@MWCNT might result from the electronic interaction between QDs and MWCNTs [17,25]. Owing to the effective electron transfer from QDs to MWCNTs, the fluorescence decay time of  $\text{PbS}_{0.75}\text{Se}_{0.25}\text{-QD@MWCNT}$  also decreased in comparison with  $\text{PbS}_{0.75}\text{Se}_{0.25}$  QDs (Figure 3d).

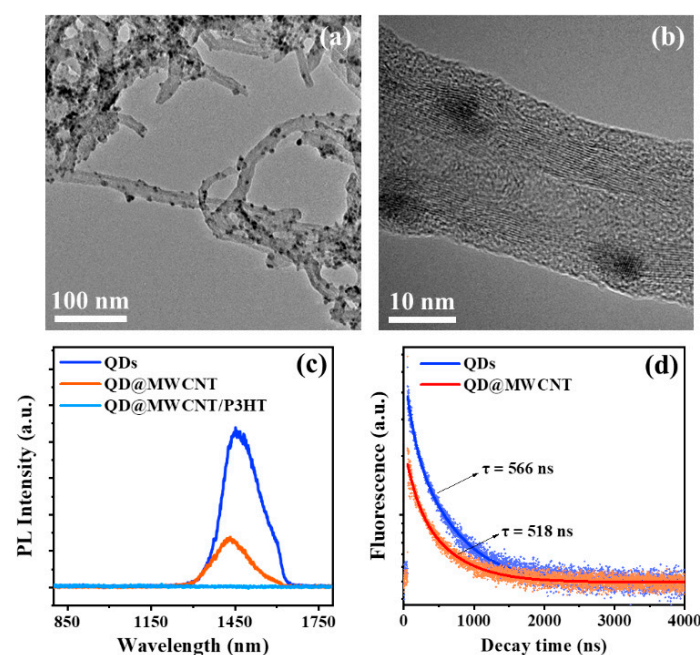


**Figure 3.** (a) TEM and (b) HRTEM images of  $\text{PbS}_{0.75}\text{Se}_{0.25}\text{-QD@MWCNT}$ . (c) PL spectra of  $\text{PbS}_{0.75}\text{Se}_{0.25}\text{-QDs}$ ,  $\text{PbS}_{0.75}\text{Se}_{0.25}\text{-QD@MWCNT}$  and  $\text{PbS}_{0.75}\text{Se}_{0.25}\text{-QD@MWCNT/P3HT}$ . (d) Fluorescence decay of  $\text{PbS}_{0.75}\text{Se}_{0.25}\text{-QDs}$  and  $\text{PbS}_{0.75}\text{Se}_{0.25}\text{-QD@MWCNT}$  with fitted curves (solid lines).



Next, we further incorporated the hole-conducting polymer P3HT into the prefabricated QD@MWCNT to form the QD@MWCNT/P3HT nanocomposite. The P3HT would recrystallize and wrap around the QD@MWCNT, forming the bulk-heterojunction-based interpenetrating network. Thus, the QD@MWCNT/P3HT nanocomposite could be expected to show an enhanced conductivity of photoinduced holes from QDs, which led to the almost completely quenched PL intensity in  $\text{PbS}_{0.75}\text{Se}_{0.25}$ -QD@MWCNT/P3HT (Figure 3c).

As shown in Figure 4a, the EIS results indicated that the conductivities were in the following sequence: QD@MWCNT/P3HT > QD@MWCNT > QD, which further confirmed the important roles of MWCNTs and P3HT in promoting the separation/transfer of photoinduced electrons and holes, respectively. The photoelectric conversion performances of QDs and QD-based nanostructures were evaluated by the I-t curves, and the photocurrents were measured to be in the following order: QD@MWCNT/P3HT > QD@MWCNT > QD > P3HT (Figure 4b). As mentioned above, while the organic conjugated P3HT could be excited under the same irradiation condition, the photocurrent intensity of P3HT was much lower than that of QDs. Therefore, the effective separation/transport of charge carriers was the main reason accounting for the enhanced photoelectric performance of  $\text{PbS}_{1-x}\text{Se}_x$ -QD@MWCNT/P3HT. The I-t curves of  $\text{PbS}_{1-x}\text{Se}_x$ -QD@MWCNT/P3HT nanocomposites with different x values were measured. Figure 4c shows the photocurrents measured at 480 s as a function of the x values in  $\text{PbS}_{1-x}\text{Se}_x$  QDs. The photocurrents measured at different times (120 s, 600 s, 720 s) showed a similar trend as that measured at 480 s (Figure S3). Clearly, the solid-solution  $\text{PbS}_{1-x}\text{Se}_x$  QDs samples possessed higher photocurrents than those of the samples based on either pure PbS or pure PbSe QDs, and the maximum photocurrent intensity was obtained for x = 0.25.

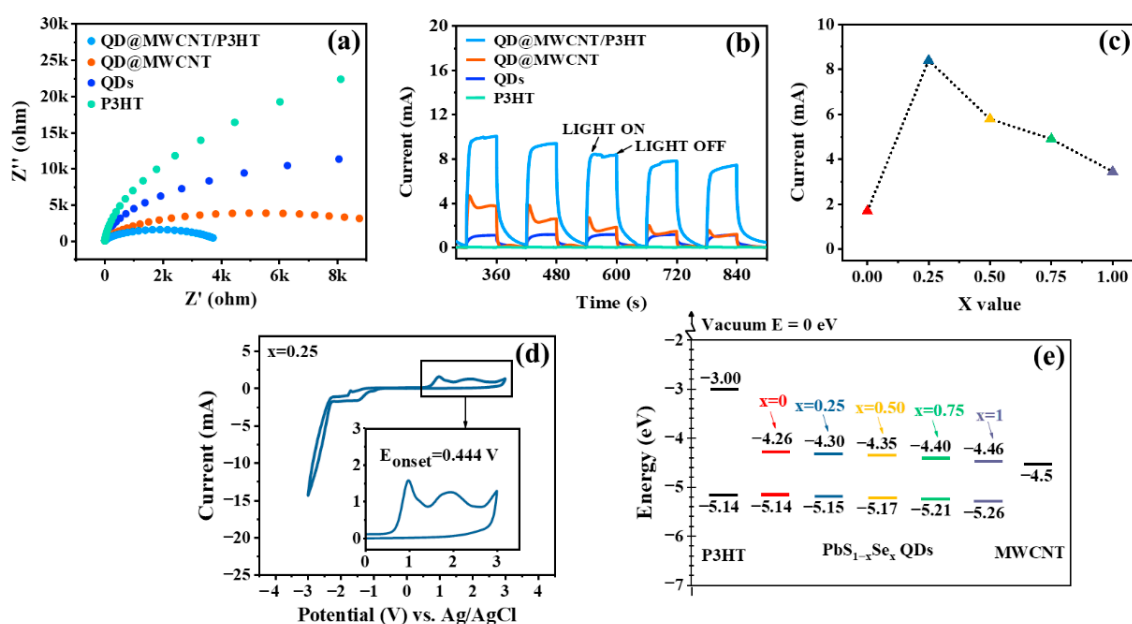


**Figure 4.** (a) EIS and (b) I-t curves of P3HT,  $\text{PbS}_{0.75}\text{Se}_{0.25}$  QDs,  $\text{PbS}_{0.75}\text{Se}_{0.25}$ -QD@MWCNT and  $\text{PbS}_{0.75}\text{Se}_{0.25}$ -QD@MWCNT/P3HT. (c) Photocurrent as a function of x value in  $\text{PbS}_{1-x}\text{Se}_x$ -QD@MWCNT/P3HT. (d) CV plot of  $\text{PbS}_{0.75}\text{Se}_{0.25}$  QDs. (e) Energy level diagram of the P3HT and  $\text{PbS}_{1-x}\text{Se}_x$  QDs. The work function of MWCNTs was referred to in the previous report [49].

The significantly improved photoelectric conversion performance of the  $\text{PbS}_{0.75}\text{Se}_{0.25}$ -QD@MWCNT/P3HT nanocomposite might be accounted for by the following reasons. Firstly, the addition of Se increased the Bohr radius without changing the size of QDs, which could make the charge carriers more delocalized and transferable. Secondly, the incorporation of Se moved both the VB and CB edges to the lower positions. On one hand, the reduced band gap of  $\text{PbS}_{1-x}\text{Se}_x$  QDs rendered effective utilization of the low-

energy photons in the long-wavelength region. On the other hand, the separation/transfer of photoinduced charge carriers in the  $\text{PbS}_{1-x}\text{Se}_x\text{-QD@MWCNT/P3HT}$  nanocomposite required a suitable energy level alignment, i.e., the CB edge of  $\text{PbS}_{1-x}\text{Se}_x$  QDs should not be too low. In this context, the  $\text{PbS}_{0.75}\text{Se}_{0.25}\text{-QD@MWCNT/P3HT}$  nanocomposite exhibited the best photoelectric performance. It has been reported that cyclic voltammetry (CV) plots could reflect the redox potentials with the ionization energy and electron affinity, and the highest occupied molecular orbital (HOMO) and lowest unoccupied molecular orbital (LUMO) of the organic polymer or the CB and VB of QDs could be estimated [48,50,51]. Figure 4d and Figure S4 show the CV curves of  $\text{PbS}_{1-x}\text{Se}_x$  QDs and P3HT, and from the derived results (Table S1), we plotted the energy level diagram in Figure 4e. Apparently, the energy cascades between the LUMO of P3HT and CB edges of all the  $\text{PbS}_{1-x}\text{Se}_x$  QDs were suitable for the flow of electrons to MWCNTs. While the VB edge of PbS QDs was close to that of the HOMO level of P3HT, the increased energy offset between the VB edges of  $\text{PbS}_{1-x}\text{Se}_x$  QDs and the HOMO of P3HT could secure the transfer of holes from QDs to P3HT because the VB edges of  $\text{PbS}_{1-x}\text{Se}_x$  QDs ( $x = 0, 0.25, 0.5, 0.75$ ) were all lower than that of PbS QDs [17,19,48].

The mechanism for the promoted separation and transfer of photoinduced electrons and holes in the  $\text{PbS}_{1-x}\text{Se}_x\text{-QD@MWCNT/P3HT}$  nanocomposite is schematically shown in Figure 5. The photoinduced electrons from QDs are captured and transported in MWCNTs, and the photoinduced holes flow into the HOMO of P3HT. The photoinduced electrons from P3HT could also be transferred to the CB of  $\text{PbS}_{1-x}\text{Se}_x$  QDs and then to MWCNTs or directly transferred from P3HT to MWCNTs. In this way, the  $\text{PbS}_{1-x}\text{Se}_x\text{-QD@MWCNT/P3HT}$  nanocomposite is endowed with an efficient separation/transfer of photoinduced charge carriers, thus exhibiting significantly enhanced photoelectric conversion performance.

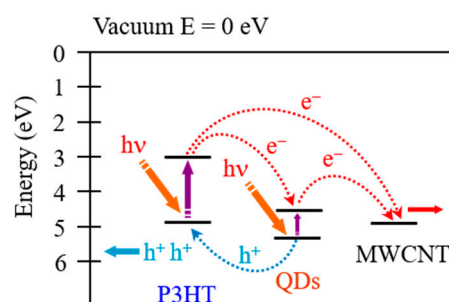


**Figure 5.** Schematic diagram of the separation and transfer of photoinduced charge carriers in the  $\text{PbS}_{1-x}\text{Se}_x\text{-QD@MWCNT/P3HT}$  nanocomposite. The work function of MWCNTs was referred to [49], and the HOMO and LUMO of P3HT were referred to in [50].

### 3. Materials and Methods

#### 3.1. Materials and Synthesis of $\text{PbS}_{1-x}\text{Se}_x$ Quantum Dots

The  $\text{PbS}_{1-x}\text{Se}_x$  ( $x = 0, 0.25, 0.5, 0.75, 1$ ) solid-solution QDs were synthesized by the classical hot-injection method under Schlenk lines to avoid damage from the oxygen and moisture. Typically, for  $\text{PbS}_{0.75}\text{Se}_{0.25}$  QDs, 0.128 g of sulfur (Alfa Aesar, Haverhill, MA, USA, 99.999%) was dissolved in 20 mL of OLA (Acros, Geel, Belgium, 80–90%) at 90 °C, while 0.316 g of selenium (Aladdin, 99.9%) was heated at 240 °C to form a brown precursor with the same amount of OLA. Then, 3.8 mL of S-OLA and 1.2 mL of Se-OLA were blended in a flask and purged with argon gas for 30 min under magnetic stirring. After that, the mixture was heated to 150 °C for 10 min. In parallel, 0.278 g of  $\text{PbCl}_2$  (Alfa Aesar, 99.999%) and 5 mL of OLA were placed into a flask and degassed for 30 min under magnetic stirring and then heated to 95 °C to form a homogenous transparent solution. The mixture of S-OLA and Se-OLA was swiftly injected into the flask containing  $\text{PbCl}_2\text{-OLA}$ , and the temperature was maintained slightly above 95 °C. After reacting for a certain time, the mixture was quenched into cold hexane to stop the growth of

PbS<sub>0.75</sub>Se<sub>0.25</sub> QDs. The solution was left at room temperature for 4 h and then centrifuged to separate and remove the unreacted PbCl<sub>2</sub> and larger black sediment. The supernatant was carefully purified by adding the least amount of ethanol with successive vibration until the solution became turbid, then a secondary centrifugation was performed to obtain the black solution. Finally, the monodispersed PbS<sub>0.75</sub>Se<sub>0.25</sub> QDs were extracted, dissolved in toluene and stored at 4 °C to slow down the defocusing in particle size distribution caused by Ostwald ripening. Following the synthesis procedure of PbS<sub>0.75</sub>Se<sub>0.25</sub> QDs, the synthesis parameters of PbS, PbS<sub>0.50</sub>Se<sub>0.50</sub>, PbS<sub>0.25</sub>Se<sub>0.75</sub> and PbSe QDs are shown in Table S2 (Supporting Information). The atomic ratios of S/Se in PbS<sub>1-x</sub>Se<sub>x</sub> (x = 0, 0.25, 0.5, 0.75, 1) were measured by XPS to be approximately consistent with the respective nominal ratios (Table S3, Supporting Information).

### 3.2. Construction of PbS<sub>1-x</sub>Se<sub>x</sub>-QD@MWCNT and PbS<sub>1-x</sub>Se<sub>x</sub>-QD@MWCNT/P3HT

Following a similar procedure as previously reported [17], OLA was used as the binding agent to connect the PbS<sub>1-x</sub>Se<sub>x</sub> QDs with MWCNTs directly. Briefly, the acid-treated multiwalled carbon nanotubes (MWCNTs, Timesnano) were first dispersed in toluene (1 mg/mL), and a certain amount of OLA was subsequently added with alternating sonication and vibration. Then, different amounts of OLA-capped PbS<sub>1-x</sub>Se<sub>x</sub> QDs (dispersed in toluene) were mixed with OLA-modified MWCNTs in toluene via successive vibration and ultrasonication to obtain the PbS<sub>1-x</sub>Se<sub>x</sub>-QD@MWCNT nanohybrid. The P3HT polymer (Rieke Metals, regioregular, 4002-E) was first dissolved in 1,2-dichlorobenzene (0.33 mg/mL) and then blended with PbS<sub>1-x</sub>Se<sub>x</sub>-QD@MWCNT solution. The as-received PbS<sub>1-x</sub>Se<sub>x</sub>-QD@MWCNT/P3HT nanocomposite solution was stirred at 40 °C for 12 h inside a glove box.

### 3.3. Structure, Morphology, and Optical Properties

The synthesized PbS<sub>1-x</sub>Se<sub>x</sub> QDs were drop-casted on glass and characterized by an X-ray diffractometer (XRD, Cu K $\alpha$  radiation source, D8 Advanced, Bruker, Rheinstetten, Germany). Morphological observation was conducted on a transmission electron microscope (TEM, JEM 2100f, JEOL, Tokyo, Japan). The surface chemical states were analyzed by X-ray photoelectron spectroscopy (XPS, ESCALAB-250Xi, ThermoFisher, Waltham, MA, USA) using C 1 s (284.8 eV) as the calibration reference. Absorption spectra of the PbS<sub>1-x</sub>Se<sub>x</sub> QDs in toluene solution were measured on a UV–vis–NIR spectrophotometer (UV 3600, Shimadzu, Kyoto, Japan). Steady-state photoluminescence (PL) and time-resolved fluorescence of the thin film of QDs on the glass substrate were characterized on a fluorospectrometer (Fluorolog-3, HORIBA, Piscataway, NJ, USA) with an excitation wavelength of 630 nm. All tests were performed under ambient conditions.

### 3.4. Measurements of Photoelectrochemical and Photoelectric Properties

The amperometric (I-t), cyclic voltammetry (CV) and electrochemical impedance spectroscopy (EIS) curves were measured on an electrochemical workstation (CHI760E, Chenhua, Shanghai, China) using the standard 3-electrode module with Ag/AgCl<sub>2</sub> (in 3.5 M KCl) as the reference electrode and Pt as the counter electrode. The PbS<sub>1-x</sub>Se<sub>x</sub> QDs in toluene were first dropped onto a clean ITO substrate in a N<sub>2</sub>-filled glove box to form the working electrode with the evaporation of solvent at room temperature. The test for CV curves was performed in an anhydrous acetonitrile (MACKLIN, 99.9%) electrolyte containing 0.1 M tetrabutylammonium tetrafluoroborate (MACKLIN, 98%) with a sweep rate of 0.1 V/s and an initial scan negative polarity from 0 V [50,51]. The tests for I-t and EIS curves were carried out in 0.25 M Na<sub>2</sub>S (MACKLIN, 99.9%) and 0.35 M Na<sub>2</sub>SO<sub>3</sub> (Acros, 98.5%) aqueous solution under a 300 W xenon lamp irradiation [52,53].

## 4. Conclusions

In summary, relatively small and uniform PbS<sub>1-x</sub>Se<sub>x</sub> solid-solution QDs were successfully synthesized via the hot-injection method using PbCl<sub>2</sub>, S/Se powders and OLA as the

precursors and solvent. The band gap and band edges of  $\text{PbS}_{1-x}\text{Se}_x$  QDs could be tuned by varying the S/Se ratio. Integration of  $\text{PbS}_{1-x}\text{Se}_x$  solid-solution QDs, MWCNTs and P3HT formed the  $\text{PbS}_{1-x}\text{Se}_x\text{-QD@MWCNT/P3HT}$  nanocomposite, which demonstrated a much higher photocurrent than the individual QDs, P3HT, and the binary  $\text{PbS}_{1-x}\text{Se}_x\text{-QD@MWCNT}$ . The highest photocurrent intensity was achieved over  $\text{PbS}_{0.75}\text{Se}_{0.25}\text{-QD@MWCNT/P3HT}$ , which had a suitable energy level alignment to provide the optimal driving force for both the electrons and holes. The incorporation of superior electron-conducting MWCNTs and hole-conducting P3HT allowed obtaining a  $\text{PbS}_{1-x}\text{Se}_x\text{-QD@MWCNT/P3HT}$  nanocomposite with efficient separation/transfer of photoinduced charge carriers, thus accounting for the enhanced photoelectric conversion efficiency. Systematic investigation into the controlled attachment of  $\text{PbS}_{1-x}\text{Se}_x$  QDs with MWCNTs is underway in our lab, and fabrication of the photovoltaic device using  $\text{PbS}_{1-x}\text{Se}_x\text{-QD@MWCNT/P3HT}$  as the photoactive component will be carried out in collaboration with other labs in the future. Our work has demonstrated that making solid-solution semiconductor QDs could be an effective approach to energy band engineering, and properly integrating QDs, carbon nanomaterials (CNTs, graphene, etc.) and conductive polymers into a nanocomposite could be a feasible strategy for the development of high-efficiency photoelectric conversion devices.

**Supplementary Materials:** The following are available online at <https://www.mdpi.com/article/10.3390/inorganics9120087/s1>. Table S1: Energy level alignment of P3HT and  $\text{PbS}_{1-x}\text{Se}_x$  QDs; Figure S1: (a)–(e) Histogram of size distribution of  $\text{PbS}_{1-x}\text{Se}_x$  QDs; Figure S2: (a)–(e) The fitting results of absorption spectra for  $\text{PbS}_{1-x}\text{Se}_x$  QDs; Figure S3: Photocurrents measured at different times as a function of  $x$  value in  $\text{PbS}_{1-x}\text{Se}_x\text{-QDs@MWCNT/P3HT}$ ; Figure S4: (a)–(e) Cyclic voltammetry (CV) tests of PbS,  $\text{PbS}_{0.50}\text{Se}_{0.50}$ ,  $\text{PbS}_{0.25}\text{Se}_{0.75}$ , PbSe QDs and P3HT, and (f) the absorption spectrum of P3HT; Table S2: Synthesis parameters of  $\text{PbS}_{1-x}\text{Se}_x$  QDs; Table S3: Atomic ratio of S/Se in  $\text{PbS}_{1-x}\text{Se}_x$  QDs measured by XPS.

**Author Contributions:** Conceptualization, D.W.; methodology, H.Z., H.H. and M.Y.; investigation, H.Z. and H.H.; data curation, H.Z. and H.H.; writing—original draft preparation, H.Z.; writing—review and editing, D.W.; supervision, D.W. and J.Y.; project administration, D.W.; funding acquisition, D.W. and J.Y. All authors have read and agreed to the published version of the manuscript.

**Funding:** This research was funded by the National Natural Science Foundation of China (51572191, 21633004).

**Acknowledgments:** The authors are grateful to Qianjin Guo for the assistance in TEM characterization.

**Conflicts of Interest:** The authors declare no conflict of interest.

## References

- Shrestha, A.; Batmunkh, M.; Tricoli, A.; Qiao, S.Z.; Dai, S. Near-Infrared Active Lead Chalcogenide Quantum Dots: Preparation, Post-Synthesis Ligand Exchange, and Applications in Solar Cells. *Angew. Chem. Int. Ed.* **2019**, *58*, 5202–5224. [CrossRef]
- Lu, H.; Carroll, G.M.; Neale, N.R.; Beard, M.C. Infrared Quantum Dots: Progress, Challenges, and Opportunities. *ACS Nano* **2019**, *13*, 939–953. [CrossRef]
- Tang, J.; Sargent, E.H. Infrared Colloidal Quantum Dots for Photovoltaics: Fundamentals and Recent Progress. *Adv. Mater.* **2011**, *23*, 12–29. [CrossRef]
- Hines, M.A.; Scholes, G.D. Colloidal PbS Nanocrystals with Size-Tunable Near-Infrared Emission: Observation of Post-Synthesis Self-Narrowing of the Particle Size Distribution. *Adv. Mater.* **2003**, *15*, 1844–1849. [CrossRef]
- Choi, M.J.; Pelayo Garcia de Arquer, F.; Proppe, A.H.; Seifitokaldani, A.; Choi, J.; Kim, J.; Baek, S.W.; Liu, M.; Sun, B.; Biondi, M.; et al. Cascade Surface Modification of Colloidal Quantum Dot Inks Enables Efficient Bulk Homojunction Photovoltaics. *Nat. Commun.* **2020**, *11*, 103. [CrossRef] [PubMed]
- Kelm, E.D.; Shukla, H.; Hinds, S.; Macneil, D.D.; Levina, L.; Sargent, E.H. Impact of Dithiol Treatment and Air Annealing on the Conductivity, Mobility, and Hole Density in PbS Colloidal Quantum Dot Solids. *Appl. Phys. Lett.* **2008**, *92*, 212105. [CrossRef]
- Liu, S.; Xiong, K.; Wang, K.; Liang, G.; Li, M.; Tang, H.; Yang, K.; Huang, Z.; Lian, L.; Tan, M.; et al. Efficiently Passivated PbSe Quantum Dot Solids for Infrared Photovoltaics. *ACS Nano* **2021**, *15*, 3376–3386. [CrossRef] [PubMed]
- Law, M.; Luther, J.M.; Song, Q.; Hughes, B.K.; Perkins, C.L.; Nozik, A.J. Structural, Optical, and Electrical Properties of PbSe Nanocrystal Solids Treated Thermally or with Simple Amines. *J. Am. Chem. Soc.* **2008**, *130*, 5974–5985. [CrossRef]
- Luther, J.M.; Law, M.; Song, Q.; Perkins, C.L.; Beard, M.C.; Nozik, A.J. Structural, Optical, and Electrical Properties of Self-Assembled Films of PbSe Nanocrystals Treated with 1,2-Ethanedithiol. *ACS Nano* **2008**, *2*, 271–280. [CrossRef]



10. Wise, F.W. Lead Salt Quantum Dots: The Limit of Strong Quantum Confinement. *Acc. Chem. Res.* **2000**, *33*, 773–780. [[CrossRef](#)]
11. Kang, I.; Wise, F.W. Electronic Structure and Optical Properties of PbS and PbSe Quantum Dots. *J. Opt. Soc. Am. B* **1997**, *14*, 1632–1646. [[CrossRef](#)]
12. Ellingson, R.J.; Beard, M.C.; Johnson, J.C.; Yu, P.; Micic, O.I.; Nozik, A.J.; Shabaev, A.; Efros, A.L. Highly Efficient Multiple Exciton Generation in Colloidal PbSe and PbS Quantum Dots. *Nano Lett.* **2005**, *5*, 865–871. [[CrossRef](#)] [[PubMed](#)]
13. Cademartiri, L.; Bertolotti, J.; Sapienza, R.; Wiersma, D.S.; Von Freymann, G.; Ozin, G.A. Multigram Scale, Solventless, and Diffusion-Controlled Route to Highly Monodisperse PbS Nanocrystals. *J. Phys. Chem. B* **2006**, *110*, 671–673. [[CrossRef](#)]
14. Zhao, H.; Chaker, M.; Ma, D. Bimodal Photoluminescence during the Growth of PbS Quantum Dots. *J. Phys. Chem. C* **2009**, *113*, 6497–6504. [[CrossRef](#)]
15. Konstantatos, G.; Howard, I.; Fischer, A.; Hoogland, S.; Clifford, J.; Klem, E.; Levina, L.; Sargent, E.H. Ultrasensitive Solution-Cast Quantum Dot Photodetectors. *Nature* **2006**, *442*, 180–183. [[CrossRef](#)] [[PubMed](#)]
16. Volkmann, M.; Meyns, M.; Lesyuk, R.; Lehmann, H.; Klinke, C. Attachment of Colloidal Nanoparticles to Boron Nitride Nanotubes. *Chem. Mater.* **2017**, *29*, 726–734. [[CrossRef](#)]
17. Wang, D.; Baral, J.K.; Zhao, H.; Gonfa, B.A.; Truong, V.; Khakani, M.E.; Izquierdo, R.; Ma, D. Controlled Fabrication of PbS Quantum-Dot/Carbon-Nanotube Nanoarchitecture and its Significant Contribution to Near-Infrared Photon-to-Current Conversion. *Adv. Funct. Mater.* **2011**, *21*, 4010–4018. [[CrossRef](#)]
18. Li, X.; Jia, Y.; Cao, A. Tailored Single-Walled Carbon Nanotube–CdS Nanoparticle Hybrids for Tunable Optoelectronic Devices. *ACS Nano* **2010**, *4*, 506–512. [[CrossRef](#)]
19. Pei, Q.; Chen, Z.; Wang, S.; Zhang, D.; Ma, P.; Li, S.; Zhou, X.; Lin, Y. PbS Decorated Multi-Walled Carbon Nanotube/Ti Mesh Films as Efficient Counter Electrodes for Quantum Dots Sensitized Solar Cells. *Sol. Energy* **2019**, *178*, 108–113. [[CrossRef](#)]
20. Jiang, X.; Schaller, R.D.; Lee, S.B.; Pietryga, J.M.; Klimov, V.I.; Zakhidov, A.A. PbSe Nanocrystal/Conducting Polymer Solar Cells with an Infrared Response to 2 Micron. *J. Mater. Res.* **2007**, *22*, 2204–2210. [[CrossRef](#)]
21. Hu, L.; Huang, S.; Patterson, R.; Halpert, J.E. Enhanced Mobility in PbS Quantum Dot Films via PbSe Quantum Dot Mixing for Optoelectronic Applications. *J. Mater. Chem. C* **2019**, *7*, 4497–4502. [[CrossRef](#)]
22. Zhao, H.; Fan, Z.; Liang, H.; Selopal, G.S.; Gonfa, B.A.; Jin, L.; Soudi, A.; Cui, D.; Enrichi, F.; Natile, M.M.; et al. Controlling Photoinduced Electron Transfer from PbS@CdS Core@Shell Quantum Dots to Metal Oxide Nanostructured Thin Films. *Nanoscale* **2014**, *6*, 7004–7011. [[CrossRef](#)]
23. Nguyen, D.T.; Sunil Sharma, S.; Chen, S.A.; Komarov, P.V.; Ivanov, V.A.; Khokhlov, A.R. Polymer–Quantum Dot Composite Hybrid Solar Cells with a Bi-continuous Network Morphology Using the Block Copolymer Poly(3-hexylthiophene)-*b*-polystyrene or its Blend with Poly(3-hexylthiophene) as a Donor. *Mater. Adv.* **2021**, *2*, 1016–1023. [[CrossRef](#)]
24. Kongkanand, A.; Tvrdy, K.; Takechi, K.; Kuno, M.; Kamat, P.V. Quantum Dot Solar Cells. Tuning Photoresponse through Size and Shape Control of CdSe–TiO<sub>2</sub> Architecture. *J. Am. Chem. Soc.* **2008**, *130*, 4007–4015. [[CrossRef](#)] [[PubMed](#)]
25. Wang, D.; Zhao, H.; Wu, N.; Khakani, M.E.; Ma, D. Tuning the Charge-Transfer Property of PbS–Quantum Dot/TiO<sub>2</sub>–Nanobelt Nanohybrids via Quantum Confinement. *J. Phys. Chem. Lett.* **2010**, *1*, 1030–1035. [[CrossRef](#)]
26. Liu, Z.; Sun, Y.; Yuan, J.; Wei, H.; Huang, X.; Han, L.; Wang, W.; Wang, H.; Ma, W. High-Efficiency Hybrid Solar Cells Based on Polymer/PbS<sub>x</sub>Se<sub>1–x</sub> Nanocrystals Benefiting from Vertical Phase Segregation. *Adv. Mater.* **2013**, *25*, 5772–5778. [[CrossRef](#)] [[PubMed](#)]
27. Nagaoka, H.; Colbert, A.E.; Strein, E.; Janke, E.M.; Salvador, M.; Schlenker, C.W.; Ginger, D.S. Size-Dependent Charge Transfer Yields in Conjugated Polymer/Quantum Dot Blends. *J. Phys. Chem. C* **2014**, *118*, 5710–5715. [[CrossRef](#)]
28. Akhtar, J.; Afzaal, M.; Banskil, M.; Podhorodecki, A.; Syperek, M.; Misiewicz, J.; Bangert, U.; Hardman, S.O.; Graham, D.M.; Flavell, W.R.; et al. Controlled Synthesis of Tuned Bandgap Nanodimensional Alloys of PbS<sub>x</sub>Se<sub>1–x</sub>. *J. Am. Chem. Soc.* **2011**, *133*, 5602–5609. [[CrossRef](#)] [[PubMed](#)]
29. Smith, D.K.; Luther, J.M.; Semonin, O.E.; Nozik, A.J.; Beard, M.C. Tuning the Synthesis of Ternary Lead Chalcogenide Quantum Dots by Balancing Precursor Reactivity. *ACS Nano* **2011**, *5*, 183–190. [[CrossRef](#)]
30. Gao, B.; Zhao, M.; Wang, Q.; Kang, K.; Xu, Z.; Zhang, H. Improved Synthesis of PbS<sub>x</sub>Se<sub>1–x</sub> Ternary Alloy Nanocrystals and their Nonlinear Optical Properties. *New J. Chem.* **2013**, *37*, 1692–1695. [[CrossRef](#)]
31. Ren, J.; Ouyang, S.; Chen, H.; Umezawa, N.; Lu, D.; Wang, D.; Xu, H.; Ye, J. Effective Mineralization of Organic Dye under Visible-Light Irradiation over Electronic-Structure-Modulated Sn(Nb<sub>1–x</sub>Ta<sub>x</sub>)<sub>2</sub>O<sub>6</sub> Solid Solutions. *Appl. Catal. B Environ.* **2015**, *168*, 243–249. [[CrossRef](#)]
32. Wang, L.; Ouyang, S.; Ren, B.; Ye, J.; Wang, D. Enhanced Photocatalytic Degradation of 2-Propanol over Macroporous GaN/ZnO Solid Solution Prepared by a Novel Sol-Gel Method. *APL Mater.* **2015**, *3*, 104414. [[CrossRef](#)]
33. Maeda, K.; Takata, T.; Hara, M.; Saito, N.; Inoue, Y.; Kobayashi, H.; Domen, K. GaN:ZnO Solid Solution as a Photocatalyst for Visible-Light-Driven Overall Water Splitting. *J. Am. Chem. Soc.* **2005**, *127*, 8286–8287. [[CrossRef](#)] [[PubMed](#)]
34. Ren, B.; Zhang, X.; Zhao, M.; Wang, X.; Ye, J.; Wang, D. Significant Enhancement in Photocatalytic Activity of (GaN)<sub>1–x</sub>(ZnO)<sub>x</sub> Nanowires via Solubility and Crystal Facet Tailoring. *AIP Adv.* **2018**, *8*, 015206. [[CrossRef](#)]
35. Wang, D.; Kako, T.; Ye, J. Efficient Photocatalytic Decomposition of Acetaldehyde over a Solid-Solution Perovskite (Ag<sub>0.75</sub>Sr<sub>0.25</sub>)(Nb<sub>0.75</sub>Ti<sub>0.25</sub>)O<sub>3</sub> under Visible-Light Irradiation. *J. Am. Chem. Soc.* **2008**, *130*, 2724–2725. [[CrossRef](#)] [[PubMed](#)]
36. Wang, D.; Kako, T.; Ye, J. New Series of Solid-Solution Semiconductors (AgNbO<sub>3</sub>)<sub>1–x</sub>(SrTiO<sub>3</sub>)<sub>x</sub> with Modulated Band Structure and Enhanced Visible-Light Photocatalytic Activity. *J. Phys. Chem. C* **2009**, *113*, 3785–3792. [[CrossRef](#)]

- 
37. Ma, W.; Luther, J.M.; Zheng, H.; Yue, W.; Alivisatos, A.P. Photovoltaic Devices Employing Ternary  $\text{PbS}_x\text{Se}_{1-x}$  Nanocrystals. *Nano Lett.* **2009**, *9*, 1699–1703. [[CrossRef](#)] [[PubMed](#)]
  38. Ma, W.; Swisher, S.L.; Ewers, T.; Engel, J.; Ferry, V.E.; Atwater, H.A.; Alivisatos, A.P. Photovoltaic Performance of Ultrasmall PbSe Quantum Dots. *ACS Nano* **2011**, *5*, 8140–8147. [[CrossRef](#)]
  39. Murray, C.B.; Kagan, C.R.; Bawendi, M.G. Synthesis and Characterization of Monodisperse Nanocrystals and Close-Packed Nanocrystal Assemblies. *Ann. Rev. Mater. Sci.* **2000**, *30*, 545–610. [[CrossRef](#)]
  40. Yuan, M.; Kemp, K.W.; Thon, S.M.; Kim, J.Y.; Chou, K.W.; Amassian, A.; Sargent, E.H. High-Performance Quantum-Dot Solids via Elemental Sulfur Synthesis. *Adv. Mater.* **2014**, *26*, 3513–3519. [[CrossRef](#)] [[PubMed](#)]
  41. Weidman, M.C.; Beck, M.E.; Hoffman, R.S.; Prins, F.; Tisdale, W.A. Monodisperse, Air-Stable PbS Nanocrystals via Precursor Stoichiometry Control. *ACS Nano* **2014**, *8*, 6363–6371. [[CrossRef](#)]
  42. Klimov, V.I. Detailed-Balance Power Conversion Limits of Nanocrystal-Quantum-Dot Solar Cells in the Presence of Carrier Multiplication. *Appl. Phys. Lett.* **2006**, *89*, 123188. [[CrossRef](#)]
  43. Thomson, J.W.; Wang, X.; Hoch, L.; Faulkner, D.; Petrov, S.; Ozin, G.A. Discovery and Evaluation of a Single Source Selenium Sulfide Precursor for the Synthesis of Alloy  $\text{PbS}_x\text{Se}_{1-x}$  Nanocrystals. *J. Mater. Chem.* **2012**, *22*, 5984–5989. [[CrossRef](#)]
  44. Yu, W.W.; Falkner, J.C.; Shih, B.S.; Colvin, V.L. Preparation and Characterization of Monodisperse PbSe Semiconductor Nanocrystals in a Noncoordinating Solvent. *Chem. Mater.* **2004**, *16*, 3318–3322. [[CrossRef](#)]
  45. Baranov, D.; Lynch, M.J.; Curtis, A.C.; Carollo, A.R.; Douglass, C.R.; Mateo-Tejada, A.M.; Jonas, D.M. Purification of Oleylamine for Materials Synthesis and Spectroscopic Diagnostics for trans Isomers. *Chem. Mater.* **2019**, *31*, 1223–1230. [[CrossRef](#)]
  46. Garcia-Gutierrez, D.F.; Hernandez-Casillas, L.P.; Cappellari, M.V.; Fungo, F.; Martínez-Guerra, E.; García-Gutiérrez, D.I. Influence of the Capping Ligand on the Band Gap and Electronic Levels of PbS Nanoparticles through Surface Atomistic Arrangement Determination. *ACS Omega* **2018**, *3*, 393–405. [[CrossRef](#)]
  47. Landes, C.; Braun, M.; Burda, C.; El-Sayed, M.A. Observation of Large Changes in the Band Gap Absorption Energy of Small CdSe Nanoparticles Induced by the Adsorption of a Strong Hole Acceptor. *Nano Lett.* **2001**, *1*, 667–670. [[CrossRef](#)]
  48. Hyun, B.; Zhong, Y.; Bartnik, A.C.; Sun, L.; Abrun, H.D.; Wise, F.W.; Goodreau, J.D.; Matthews, J.R.; Leslie, T.D.; Borrelli, N.F. Electron Injection from Colloidal PbS Quantum Dots into Titanium Dioxide Nanoparticles. *ACS Nano* **2008**, *2*, 2206–2212. [[CrossRef](#)] [[PubMed](#)]
  49. Chen, L.; Pan, X.; Zheng, D.; Gao, Y.; Jiang, X.; Xu, M.; Chen, H. Hybrid Solar Cells Based on P3HT and Si@MWCNT Nanocomposite. *Nanotechnology* **2010**, *21*, 345201. [[CrossRef](#)]
  50. Solomeshch, O.; Kigel, A.; Saschiuk, A.; Medvedev, V.; Aharoni, A.; Razin, A.; Eichen, Y.; Banin, U.; Lifshitz, E.; Tessler, N. Optoelectronic Properties of Polymer-Nanocrystal Composites Active at Near-Infrared Wavelengths. *J. Appl. Phys.* **2005**, *98*, 074310. [[CrossRef](#)]
  51. Kucur, E.; Riegler, J.; Urban, G.A.; Nann, T. Determination of Quantum Confinement in CdSe Nanocrystals by Cyclic Voltammetry. *J. Chem. Phys.* **2003**, *119*, 2333–2337. [[CrossRef](#)]
  52. Pathak, P.; Podzorski, M.; Bahnemann, D.; Subramanian, V.R. One-Pot Fabrication of High Coverage PbS Quantum Dot Nanocrystal-Sensitized Titania Nanotubes for Photoelectrochemical Processes. *J. Phys. Chem. C* **2018**, *122*, 13659–13668. [[CrossRef](#)]
  53. Zhang, R.; Luo, Q.; Chen, H.; Yu, X.; Kuang, D.; Su, C. CdS/CdSe Quantum Dot Shell Decorated Vertical ZnO Nanowire Arrays by Spin-Coating-Based SILAR for Photoelectrochemical Cells and Quantum-Dot-Sensitized Solar cells. *ChemPhysChem* **2012**, *13*, 1435–1439. [[CrossRef](#)] [[PubMed](#)]